

Unsupervised event identification and tagging for diffraction focusing

Alexander Bauer¹, Benjamin Schwarz², Tobias Werner¹ and Dirk Gajewski¹

¹*Institute of Geophysics, University of Hamburg, Bundesstraße 55, D-20146 Hamburg, Germany. E-mail: alex.bauer@uni-hamburg.de*

²*Department of Earth Sciences, University of Oxford, South Parks Road, Oxford OX1 3AN, UK*

Accepted 2019 February 22. Received 2018 December 4; in original form 2018 July 19

SUMMARY

Multiparameter stacking schemes like the common-reflection-surface (CRS) stack have shown to yield reliable results even for strongly noise-contaminated data. This is particularly useful for low-amplitude events such as diffractions, but also in passive seismic settings. As a by-product to a zero-offset section with a significantly improved signal-to-noise ratio, the CRS stack also extracts a set of physically meaningful wavefront attributes from the seismic data, which are a powerful tool for further data analysis. These wavefront attributes describe the properties of two conceptual wavefronts emerging at the surface. While these wavefronts are hypothetical in the reflection case, for diffractions and passive seismic events the wavefront attributes describe the actually measured wavefront. Although the attributes are extracted locally from the raw data and vary laterally along the events, an analysis of their local similarity allows the global identification of measurements that stem from the same diffractor or passive source, that is, from the same location in the subsurface. In this work, we present a fully unsupervised scheme to globally identify and tag diffractions in simple and complex data by means of local attribute similarity. Due to the fact that wave propagation is a smooth process and due to the assumption of only local attribute similarity, this approach is not restricted to settings with moderate subsurface heterogeneity. We demonstrate by means of a simple example that event tagging is an essential ingredient for, for example, focusing analysis in wavefront tomography and for uncertainty analysis of velocity and localization for diffraction-only data. Although not explicitly shown in this work, the proposed method is equally applicable to passive seismic data.

Key words: Controlled source seismology; Image processing; Seismic tomography; Wave scattering and diffraction.

1 INTRODUCTION

In recent years, the process of seismic diffraction has gained increasing research interest in hydrocarbon exploration because it is known to be caused by small subsurface heterogeneities often related to complicated geology (e.g. Landa & Keydar 1998). In that context, the successful focusing of recorded diffractions bears the potential for very localized, highly resolved imaging of discontinuous changes in elastic properties of the subsurface that naturally complements more conventional laterally smooth reflection images (Khaidukov *et al.* 2004). As one of the first objectives, seismic diffractions have been successfully used to identify and image faults, which are often poorly resolved (Krey 1952). In addition to increased resolution, the successful incorporation of diffracted arrivals in velocity model building schemes has recently suggested that another major benefit of these weak signatures is improved lateral illumination of subsurface structures, which makes them particularly useful in reduced cost-effective acquisitions (Fomel *et al.* 2007; Santos *et al.* 2012; Bauer *et al.* 2017a).

Despite all the aforementioned principal advantages of diffracted wavefields, they still remain largely unexplored in common processing workflows. Aside from the overall weakness of these signals' amplitudes, the main reason for this systematic neglect arguably arises from the fact that they strongly interfere with other more prominent wavefield contributions, in particular reflections (e.g. Kozlov *et al.* 2004). Because of that, in recent years, a variety of methods has been suggested to robustly separate the weak diffraction background. However, as many of these approaches depend on the *a priori* knowledge of a depth–velocity model, they can only indirectly contribute to velocity model building (e.g. Moser & Howard 2008; Klovok & Fomel 2012; Dafni & Symes 2017) and diffraction separation remains a direction of active research. Together with different variations of plane-wave destruction filters (Fomel 2002), notable advances have been made in utilizing collective event properties, linked to characteristics of the emerging wavefronts, for diffraction identification, extraction and imaging. Building on the assumption of local coherence, multiparameter stacking schemes such as the common-reflection-surface (CRS) stack (Jäger *et al.* 2001) not only provide an improved data volume

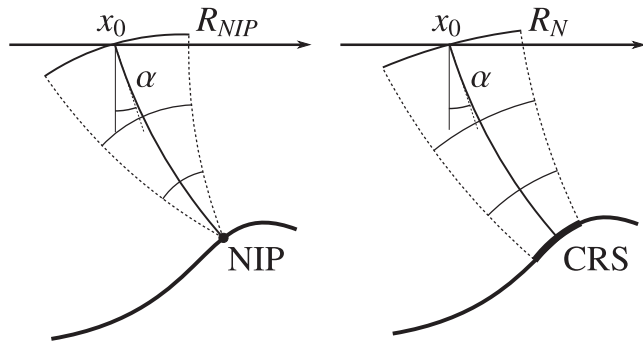


Figure 1. The 2D wavefront attributes α , R_{NIP} and R_N . In the reflection case, the NIP wave (left) is excited by a point source placed on the reflector's point of normal incidence (NIP) and the normal wave (right) is excited by an exploding reflector segment (CRS) around the NIP. In the case of a diffraction or a passive seismic event, they coincide and describe the actually measured wavefront.

with a significantly increased signal-to-noise ratio but also extract a set of physically meaningful wavefront attributes from the data. These wavefront attributes (Hubral 1983) can be used for numerous subsequent processing steps, such as time migration (e.g. Mann 2002; Bóna 2011), pre-stack data enhancement (Baykulov & Gajewski 2009), pre-stack diffraction enhancement (Bauer et al. 2016), diffraction separation (Dell & Gajewski 2011; Schwarz & Gajewski 2017b; Bakhtiari Rad et al. 2018) and velocity model building for reflection (Duveneck 2004a) and diffraction (Bauer et al. 2017a), as well as passive seismic data (Schwarz et al. 2016; Diekmann et al. 2018).

Also, it has been suggested that from a wavefront perspective, diffractions behave kinematically exactly like passive sources excited at the diffracting structure in depth, which makes most of the aforementioned processing schemes likewise naturally applicable to diffracted and passive events (Schwarz et al. 2016, 2017; Diekmann et al. 2018). Consequently, all of these applications would benefit from the *a priori* knowledge, which wavefront measurements share the same origin in depth. While this discrimination can be easily made with the human eye by optically tracking the diffracted or passive event, an algorithm requires objective criteria for the identification and discrimination of contributions stemming from different subsurface regions. Following the mentality of image segmentation, which is routinely employed in image processing workflows, in this work, we propose a fully unsupervised scheme, which utilizes the local similarity of wavefront attributes for the global identification and tagging of diffractions directly in the data domain. Since wave propagation is a smooth process, the assumption of local similarity of wavefront attributes is reasonable and not restricted to settings with moderate subsurface heterogeneity.

In the following section, we introduce the theory of wavefront attributes, whose understanding is fundamental for the proposed method. We outline various applications of them, which partly are a requirement for event tagging. After that, we introduce the event tagging scheme in theory and by means of a simple synthetic example. We then confirm the stability of the proposed method by means of simple synthetic 2D and 3D diffraction examples and an application to complex 2D marine field data. Further, we suggest a range of applications—including the formulation of focusing constraints in wavefront tomography or the assessment of event-consistent location and velocity inversion uncertainties—directly

following or benefiting from the suggested automated classification strategy.

2 WAVEFRONT ATTRIBUTES

Wavefront attributes (Hubral 1983) are physically meaningful parameters, which are encoded in the moveout of seismic events. They describe the direction and the radii of two conceptual waves emerging at the recording surface at the angle α . While the normal-incidence-point (NIP) wave is excited by a hypothetical point source placed on the reflector's point of normal incidence, the normal (N) wave is excited by a hypothetical exploding reflector segment around the NIP. In the case of a point diffraction or a passive event, the two waves coincide. In addition, the NIP wave is no longer hypothetical as it describes the wavefront that actually emerges at the recording surface. In Fig. 1, the meaning of the three 2D wavefront attributes is illustrated. In 3D, the concept of the two waves is the same, but the number of parameters increases to eight.

2.1 Common-reflection surface

The wavefront attributes can be extracted from the raw data by the application of multiparameter stacking methods such as the CRS stack (Jäger et al. 2001) using local (Mann 2002) or global (Walda & Gajewski 2017) optimization methods. In 2D, the hyperbolic CRS stacking operator reads

$$t^2(t_0, x_0) = (t_0 + 2p\Delta x)^2 + 2t_0(M_{NIP}h^2 + M_N\Delta x^2), \quad (1)$$

where the midpoint displacement $\Delta x = x - x_0$ is the distance from the central midpoint x_0 and h is the half-offset. The first derivative of the traveltimes moveout is the horizontal slowness, which can be related to the emergence angle α of the locally measured wavefront,

$$p = \frac{\sin \alpha}{v_0}, \quad (2)$$

where v_0 is the near-surface velocity. The second derivatives of the traveltimes moveout with respect to half-offset and midpoint displacement, respectively, contain the wavefront curvatures R_{NIP} and R_N of the two previously mentioned hypothetical waves (Hubral 1983):

$$M_{NIP} = \frac{\cos^2 \alpha}{v_0 R_{NIP}}, \quad M_N = \frac{\cos^2 \alpha}{v_0 R_N}. \quad (3)$$

In addition to CRS, numerous other multi-parameter traveltimes formulations exist, which are either hyperbolic (Jäger et al. 2001) or non-hyperbolic (Gelchinsky et al. 1999; Fomel & Kazinnik 2013; Schwarz et al. 2014). However, all of them may be parametrized in terms of the previously introduced wavefront attributes. Further, recent studies for heterogeneous subsurface settings have shown that wavefront attributes of good quality can be obtained with either of them (Schwarz & Gajewski 2017a,c; Walda et al. 2017).

In practice, the wavefront attributes are extracted from the data in an automatic fashion by searching the set of attributes (α , R_{NIP} , R_N) at a point in the data, which yields the largest local semblance coefficient for a subset of traces located in a pre-defined aperture extending in midpoint and half-offset direction around a central point (t_0, x_0) . This optimization problem can be solved either by three 1-D line searches and a subsequent local optimization (Mann 2002) or by a global optimization with a simultaneous search for all three attributes (Walda & Gajewski 2017).

In the 3D case, the hyperbolic CRS traveltime moveout is given by (e.g., Müller 2009)

$$t^2(t_0, \mathbf{m}_0) = (t_0 + 2\mathbf{p}\Delta\mathbf{m})^2 + 2t_0(\mathbf{h}^T\mathbf{M}\mathbf{h} + \Delta\mathbf{m}^T\mathbf{N}\Delta\mathbf{m}), \quad (4)$$

where the vectors $\Delta\mathbf{m} = \mathbf{m} - \mathbf{m}_0$ and \mathbf{h} denote the midpoint displacement and half-offset, respectively. The slowness vector \mathbf{p} contains the two angles that define the emergence direction of the previously introduced conceptual wavefronts, the NIP wave and the normal wave, which are described by the symmetric 2×2 matrices \mathbf{M} and \mathbf{N} . Accordingly, in the 3D case eight wavefront attributes have to be extracted from the data. In the diffraction case, this number reduces to five, because \mathbf{M} and \mathbf{N} coincide.

2.2 Applications of wavefront attributes

Since the wavefront attributes estimated during the CRS stack have a physical meaning, they can be exploited for numerous subsequent applications, some of which we will briefly introduce in the following. All of these applications are directly connected to the event tagging scheme suggested in this work. While the application of diffraction filters for active seismic data is a prerequisite for the event tagging, methods like pre-stack data enhancement, time migration and wavefront tomography can benefit from the previous identification and tagging of measurements with common origin in depth.

2.2.1 Diffraction separation

Diffractions are often hidden or masked by reflections, which usually have larger amplitudes. However, as they are caused by small subsurface heterogeneities, they often contain structurally relevant information, which is necessary to obtain detailed images of the subsurface. Therefore, the separation of diffractions is an important application. For that, we can make use of the fact that in the case of a diffraction, the two wavefront curvatures R_{NIP} and R_{N} coincide. Dell & Gajewski (2011) introduced the threshold function

$$w_R(t_0, x_0) = \exp\left(-\frac{|R_{\text{N}} - R_{\text{NIP}}|}{|R_{\text{N}} + R_{\text{NIP}}|}\right), \quad (5)$$

which takes the value one if $R_{\text{NIP}} = R_{\text{N}}$ and is smaller if they differ. Thus, by defining a threshold close to one and only stacking those events for which the threshold is exceeded, it is possible to obtain a stacked section that predominantly contains diffracted energy.

A different approach for the separation of diffractions was recently introduced by Schwarz & Gajewski (2017b). It is designed for low-fold or single-channel data, as often acquired in academic environments, where the wavefront curvatures cannot be estimated accurately because of the missing offsets. Therefore, the separation of reflections and diffractions requires a different filter function in this case. Schwarz & Gajewski (2017b) suggest to generate reflection-only data, which can then be subtracted adaptively from the original data in order to generate diffraction-only data. They use a filter function

$$F_p(|p|) = 1 - \Theta(|p| - |p_0|), \quad (6)$$

where Θ is the Heaviside step function. Here, p_0 represents a user-defined threshold, which can be chosen relatively small for moderate reflector dips. In contrast to the second-order diffraction filter (5), the function F_p becomes one for reflections and can thus be used to generate reflection-only data \mathcal{R} . The reflection-only data \mathcal{R} can then be subtracted adaptively from the input data \mathcal{I} , resulting in

diffraction-only data \mathcal{D} (Schwarz & Gajewski 2017b),

$$\mathcal{D}(t_0, x_0) = \mathcal{I}(t_0, x_0) - \gamma \mathcal{R}(t_0 + \tau, x_0), \quad (7)$$

where γ is a local scaling coefficient and τ a time correction. These quantities are the result of an optimization problem, which has to be solved for every data point (t_0, x_0) .

2.2.2 Pre-stack data enhancement

The zero-offset wavefront attributes may also be used for pre-stack data enhancement without explicitly performing computationally expensive finite-offset stacks (Baykulov & Gajewski 2009; Schwarz *et al.* 2015; Bauer *et al.* 2016). In the partial CRS stack (Baykulov & Gajewski 2009), the reference traveltime t_0 is extrapolated to finite offset and the zero-offset wavefront attributes are used to perform local finite-offset stacks in the pre-stack data without any further optimization. For moderate heterogeneity and small stacking apertures this method can provide regularized pre-stack data with a significantly increased signal-to-noise ratio, which is particularly helpful in the case of low-fold land data with irregular acquisition and strong noise. Schwarz *et al.* (2015) extended this method by extrapolating not only t_0 , but also the slopes to finite-offset. They use the first-order finite-offset traveltime operator (Zhang *et al.* 2001) for a local refinement of the extrapolated slopes and perform local finite-offset stacks with the obtained attributes.

2.2.3 Time migration

Time migration is a widely used method for obtaining a first structural image of the subsurface. While depth migration, which is the final step of seismic imaging, is very sensitive to errors in the velocity model, time migration is far less sensitive to velocity errors. Mann (2002) introduced a way to estimate the apex location of a diffractor in time based on the zero-offset wavefront attributes. The apex coordinates can be obtained in the zero-offset plane ($h = 0$) by setting the derivative of the traveltime moveout of a diffraction (eq. 1 with $M_{\text{N}} = M_{\text{NIP}}$) with respect to the midpoint direction to zero,

$$t_{\text{apex}}^2(t_0, x_0) = \frac{t_0^3 v_0 \cos^2 \alpha}{2R_{\text{NIP}} \sin^2 \alpha + t_0 v_0 \cos^2 \alpha}, \quad (8)$$

$$x_{\text{apex}}(t_0, x_0) = x_0 - \frac{R_{\text{NIP}} t_0 v_0 \sin \alpha}{2R_{\text{NIP}} \sin^2 \alpha + t_0 v_0 \cos^2 \alpha}, \quad (9)$$

$$v_{\text{RMS}}^2(t_0, x_0) = \frac{2v_0^2 R_{\text{NIP}}}{2R_{\text{NIP}} \sin^2 \alpha + t_0 v_0 \cos^2 \alpha}, \quad (10)$$

where $(t_{\text{apex}}, x_{\text{apex}})$ are the estimated apex coordinates for the considered event at (t_0, x_0) and v_{RMS} the corresponding dip-corrected effective velocity. The apex coordinates are constant along an event in the case of no lateral heterogeneity. Still, also in a heterogeneous subsurface they should not vary much along a diffraction and thus are a helpful tool for the global identification of events.

3 EVENT TAGGING

Although the zero-offset wavefront attributes obtained during the application of the CRS stack are local quantities, they provide us with valuable information about the measured events that can be exploited for the automatic global identification and tagging of events with a common origin in depth. Since wave propagation is

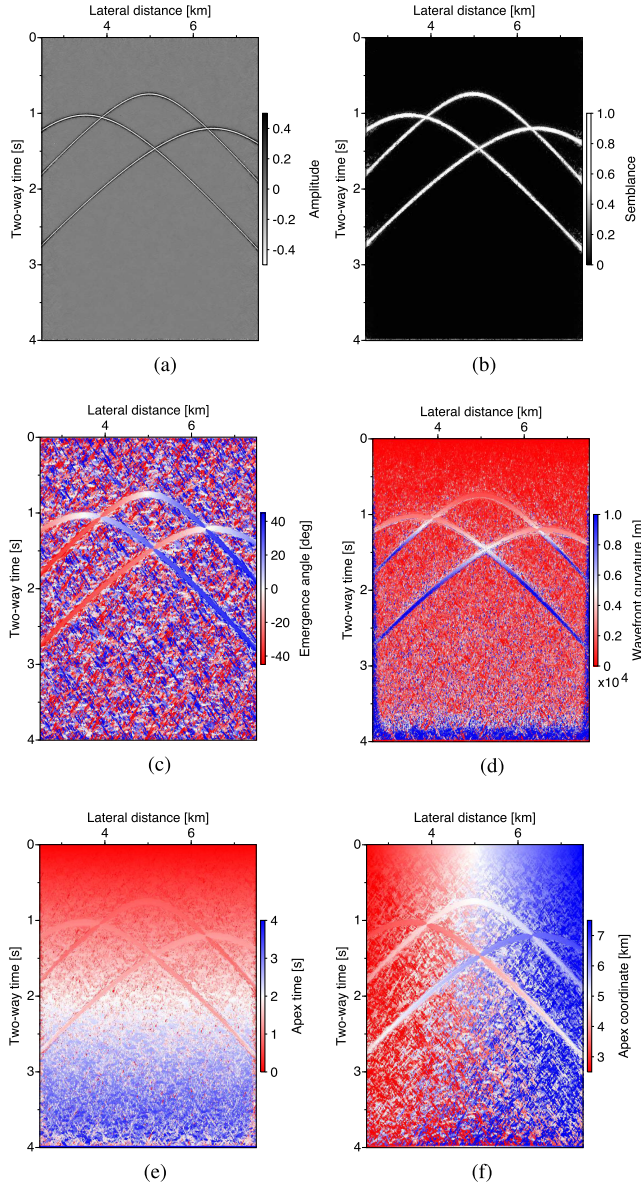


Figure 2. Zero-offset sections for simple synthetic diffraction data with three events. The first line shows (a) the zero-offset CRS stack and (b) the corresponding semblance. The second line shows the wavefront attributes (c) α and (d) R_{NIP} estimated during the CRS stack. The apex coordinates (e) t_{apex} and (f) x_{apex} are calculated from the wavefront attributes.

a smooth process, it is reasonable to assume the local similarity of wavefront attributes, that is, that wavefront attributes do not change abruptly along an event. Due to this assumption of only local similarity, the global identification of events is not limited to data acquired in subsurface settings with a small degree of heterogeneity. Accordingly, the goal of our method is an automatic analysis of the diffractions in a given set of zero-offset wavefront attributes resulting in the assignment of a numeric tag to each unique event. The method consists of two main steps which we will outline in the following with the help of a simple synthetic diffraction data example.

3.1 Detection of events

Fig. 2 shows zero-offset sections for a simple synthetic 2D diffrac-

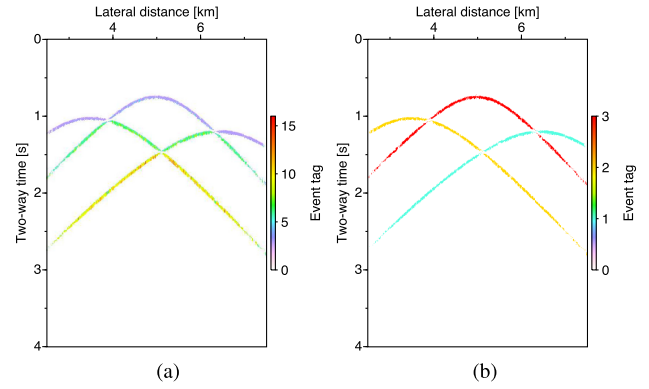


Figure 3. Event tags for the simple synthetic diffraction data: (a) the trace-wise detected events and (b) the final event tags after the lateral matching of the detected events.

tion data set, which contains three diffractions and is based on a velocity model containing both vertical and lateral heterogeneity. In the upper two rows of Fig. 2, the results from the CRS stack are displayed: the zero-offset stack (Fig. 2a), the corresponding coherence (Fig. 2b) and the wavefront attributes α (Fig. 2c) and R_{NIP} (Fig. 2d). The bottom line of Fig. 2 shows the apex coordinates t_{apex} (Fig. 2e) and x_{apex} (Fig. 2f) calculated from the wavefront attributes via eqs (8) and (9), respectively. As expected, although α and R_{NIP} vary strongly along the diffractions, they are locally smooth and do not experience abrupt changes. Therefore, the assumption of local similarity is valid and we can utilize it for the global identification of events. The apex coordinates remain almost constant along the events and thus are a suitable additional criterion for the identification of events. We suggest to use the semblance and all four attributes for the matching of events in order to better constrain the problem.

The first step of the event tagging consists in the automatic detection of ‘valid’ events, which is carried out trace-wise. For this purpose, we define a window τ_{max} around a given central sample t_0 , such that the time range $t_0 \pm \tau_{max}$ is considered. The value for τ_{max} should be chosen such that the total length of the window is smaller than the width of the events in the coherence section. The given sample t_0 is only considered if its coherence exceeds a pre-defined threshold. If this is the case, we evaluate the local similarity of the wavefront attributes by calculating their semblance coefficients (Neidell & Taner 1971) given by

$$S_\phi(t_0, x_0) = \frac{1}{n} \frac{\left(\sum_{\tau=t_0-\tau_{max}}^{t_0+\tau_{max}} \phi(\tau, x_0) \right)^2}{\sum_{\tau=t_0-\tau_{max}}^{t_0+\tau_{max}} \phi(\tau, x_0)^2}, \quad (11)$$

where ϕ is the corresponding wavefront attribute (α , R_{NIP} , x_{apex} or t_{apex}), x_0 is the midpoint under consideration and n is the number of samples in the window. In the case of a valid event, which usually ranges over various samples, the local similarities S_ϕ of the attributes should be close to 1 at the event’s central sample. If the local similarities of all attributes exceed the corresponding pre-defined thresholds, which should be chosen close to 1, an event tag is assigned to the sample t_0 under consideration. If an event tag exists within the window $t_0 - \tau_{max}$, the corresponding attribute values are compared directly by calculating

$$S_\phi^{match} = \frac{1}{2} \frac{(\phi(t_0, x_0) + \phi(t_0 - \tau, x_0))^2}{\phi(t_0, x_0)^2 + \phi(t_0 - \tau, x_0)^2}, \quad (12)$$

where $\phi(t_0, x_0)$ is the wavefront attribute at the current sample t_0 and $\phi(t_0 - \tau, x_0)$ is the one at the sample $t_0 - \tau$ within the window t_0

$-\tau_{\max}$, which also contains an event tag. If S_{ϕ}^{match} is close to 1 for all attributes, the samples t_0 and $t_0 - \tau$ are assumed to belong to the same event and the tag from the sample $t_0 - \tau$ is copied to the sample t_0 . Otherwise, a new tag is assigned to the event detected on the sample t_0 . This procedure is repeated for all samples on the trace and for all traces in the zero-offset volumes. After detecting the events on all traces, we calculate the similarity of the assigned tags S_{tags} via eq. (11), which will be needed for the lateral matching of events. The result of this first step for the simple synthetic diffraction data is displayed in Fig. 3(a). It shows that the three diffractions could be detected trace-wise throughout the whole section. As a next step, these detected events have to be matched laterally. During this step, detected events with only few occurrences, that is, outliers, will be sorted out.

3.2 Lateral matching of events

The next step after the trace-wise identification of events is the lateral matching of those measurements, which belong to the same diffraction. For that, we define two windows: a window Δx_{\max} in midpoint direction, which defines the maximum number of neighbouring traces to be searched, and a window τ_{\max} in sample direction, which defines the range of time samples to be examined. The search is started at a given sample t_0 on a midpoint trace x_0 , which contains a previously identified event, that is, S_{tags} is close to 1, and coincides with a local coherence maximum, that is, the coherence at (t_0, x_0) is larger than at the surrounding samples. If this *seed event* at (t_0, x_0) has been matched in a previous search, we will only search for matching events to the right using the already assigned tag. Otherwise, we will first search for matching events to the left. During both searches, we vertically shift the search window depending on the local moveout Δt in the zero-offset section ($h = 0$), which we calculate via

$$\Delta t(t_0, x_0) = \sqrt{(t_0 + p\Delta x)^2 + M_{\text{NIP}}\Delta x^2} - t_0, \quad (13)$$

where the midpoint displacement Δx is the distance $|\Delta x| \leq \Delta x_{\max}$ from the central trace x_0 . If (t_0, x_0) has not been assigned an event tag yet, we first step trace by trace to the left ($\Delta x < 0$) while vertically shifting the search window τ_{\max} depending on the event's moveout for the given lateral distance. For each previously matched event contained in the search space, we compare its wavefront attributes to the ones of the seed event at (t_0, x_0) by calculating

$$S_{\phi}^{\text{match}} = \frac{1}{2} \frac{(\phi(t_0, x_0) + \phi(t_0 + \Delta t + \tau, x_0 + \Delta x))^2}{\phi(t_0, x_0)^2 + \phi(t_0 + \Delta t + \tau, x_0 + \Delta x)^2}, \quad (14)$$

where $\phi(t_0, x_0)$ is a wavefront attribute of the current event and $\phi(t_0 + \Delta t + \tau, x_0 + \Delta x)$ a wavefront attribute on the trace $x_0 + \Delta x$ at the sample $t_0 + \Delta t + \tau$ within the moveout-shifted vertical window $(t_0 + \Delta t) \pm \tau_{\max}$. If S_{ϕ}^{match} exceeds the pre-defined thresholds for all attributes, the measurements at (t_0, x_0) and $(t_0 + \Delta t + \tau, x_0 + \Delta x)$ are assumed to belong to the same event. If various matching events are found during the search to the left, the one with the highest matching coefficients S_{ϕ}^{match} is chosen and the event tag is copied from the corresponding location $(t_0 + \Delta t + \tau, x_0 + \Delta x)$ to (t_0, x_0) . If there are no traces to the left or the target regions of the neighbouring traces do not contain previously matched events, a new event tag is assigned to the current sample (t_0, x_0) .

As a next step, the traces to the right ($\Delta x > 0$) of the seed event at (t_0, x_0) are searched for matching events. For each event identified during step 1 within the moveout-adapted search space to the right, the wavefront attributes of the seed event at (t_0, x_0) are compared to

the ones at the corresponding location $(t_0 + \Delta t + \tau, x_0 + \Delta x)$. If S_{ϕ}^{match} exceeds the thresholds for all attributes, the current event tag is copied from (t_0, x_0) to $(t_0 + \Delta t + \tau, x_0 + \Delta x)$.

After searching all traces of the zero-offset sections for matching events, we obtain a section with a unique tag assigned to each diffraction or passive event. Events occurring on very few traces are considered outliers and sorted out. The result for the simple synthetic diffraction data is displayed in Fig. 3(b). As desired, all three diffractions could be identified globally by assigning them a unique tag. Note that this result was obtained in a fully unsupervised fashion. Applications of the event tagging algorithm to synthetic diffraction data with more events and to field data are presented in Section 4 of this paper.

3.3 Event tagging in 3D

The current implementation of the event tagging algorithm in 3D is based on the 2D implementation. However, in the current version, absolute attribute differences instead of the semblance coefficient are used for the analysis of attribute similarity. Since seismic diffractions are intrinsically 3D phenomena, the step from 2D to 3D is a natural one. While the larger number of wavefront attributes in 3D is an advantage because the discrimination of different events is better constrained, on the other hand wavefront attributes are more difficult to obtain in a stable fashion in 3D due to the same reason. We present first promising results of an application of the 3D event tagging algorithm to synthetic diffraction data in Section 4.

4 EXAMPLES

In this section we present applications of the introduced event tagging algorithm to synthetic 2D and 3D diffraction data as well as complex 2D marine field data.

4.1 2D synthetic diffraction data

The results of the application of the 2D event tagging algorithm to synthetic diffraction data containing eight diffractions are presented in Fig. 4. The diffraction-only data set is based on a vertically inhomogeneous velocity model with a velocity gradient of 0.5 s^{-1} . Fig. 4(a) shows the zero-offset coherence and Figs 4(b) and (c) show the wavefront attributes α and R_{NIP} , respectively, as resulting from the application of the CRS stack. The apex coordinates calculated via eqs (8) and (9) are displayed in Figs 4(d) and (e). All wavefront attributes reveal the expected smooth behaviour, which permits the assumption of their local similarity. The result of the application of the introduced event tagging algorithm to the shown zero-offset sections is presented in Fig. 4(f). All eight diffractions contained in the data could be discriminated and were assigned with a unique event tag. Difficulties merely occurred on the tails of the two diffractions in the upper left of the section. These two diffractions lie so close together that a discrimination is hardly possible because the wavefront attributes are practically the same, particularly on the tails. Since this also means that the two diffractions stem from almost the same subsurface region, this is not a critical problem, though.

4.2 3D synthetic diffraction data

Fig. 5 presents the results of the application of the 3D event tag-

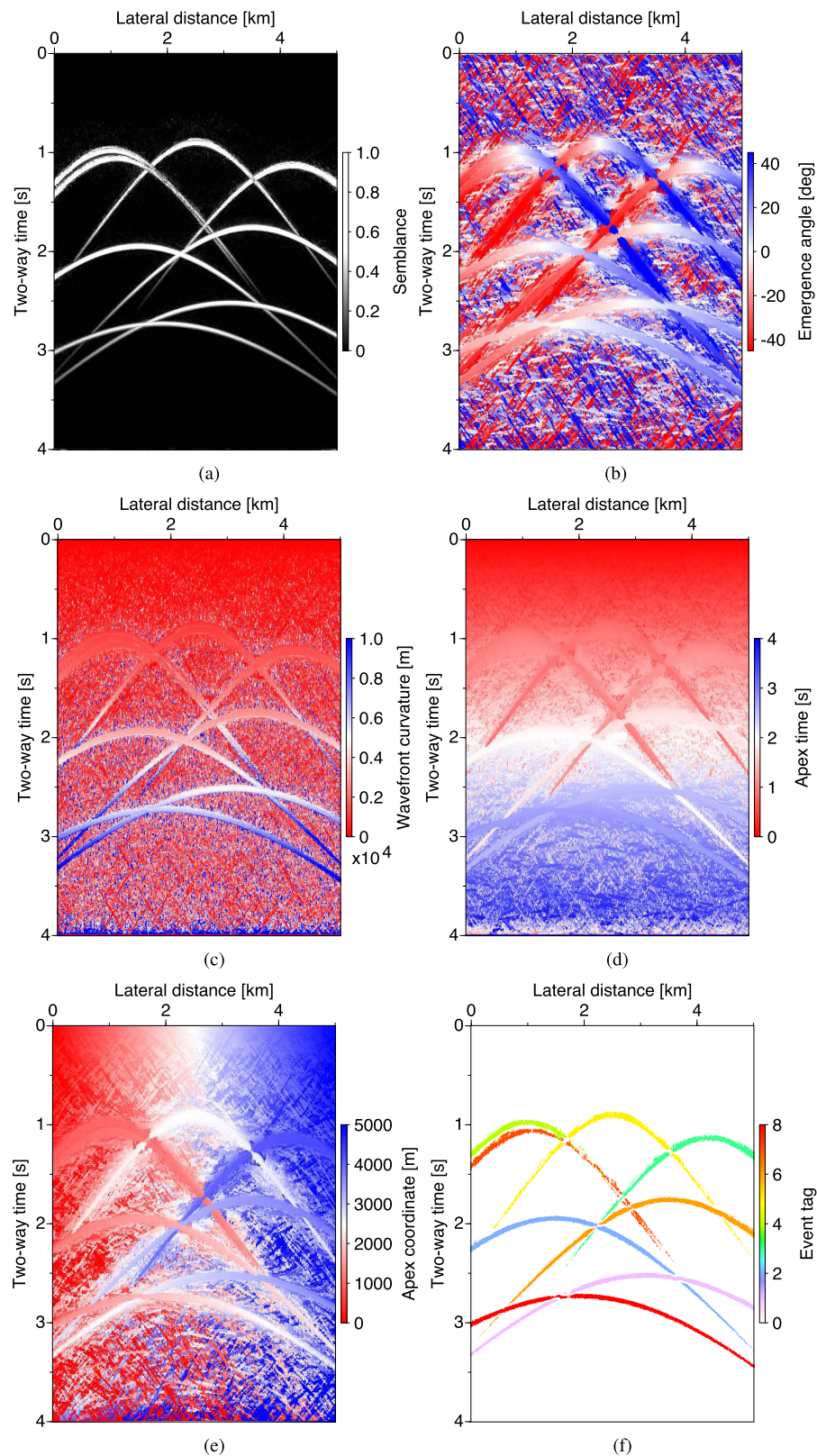


Figure 4. Results for 2D synthetic diffraction data with eight events: (a) the zero-offset coherence, the wavefront attributes (b) α and (c) R_{NIP} ; the apex coordinates (d) t_{apex} and (e) x_{apex} ; and (f) the resulting event tags.

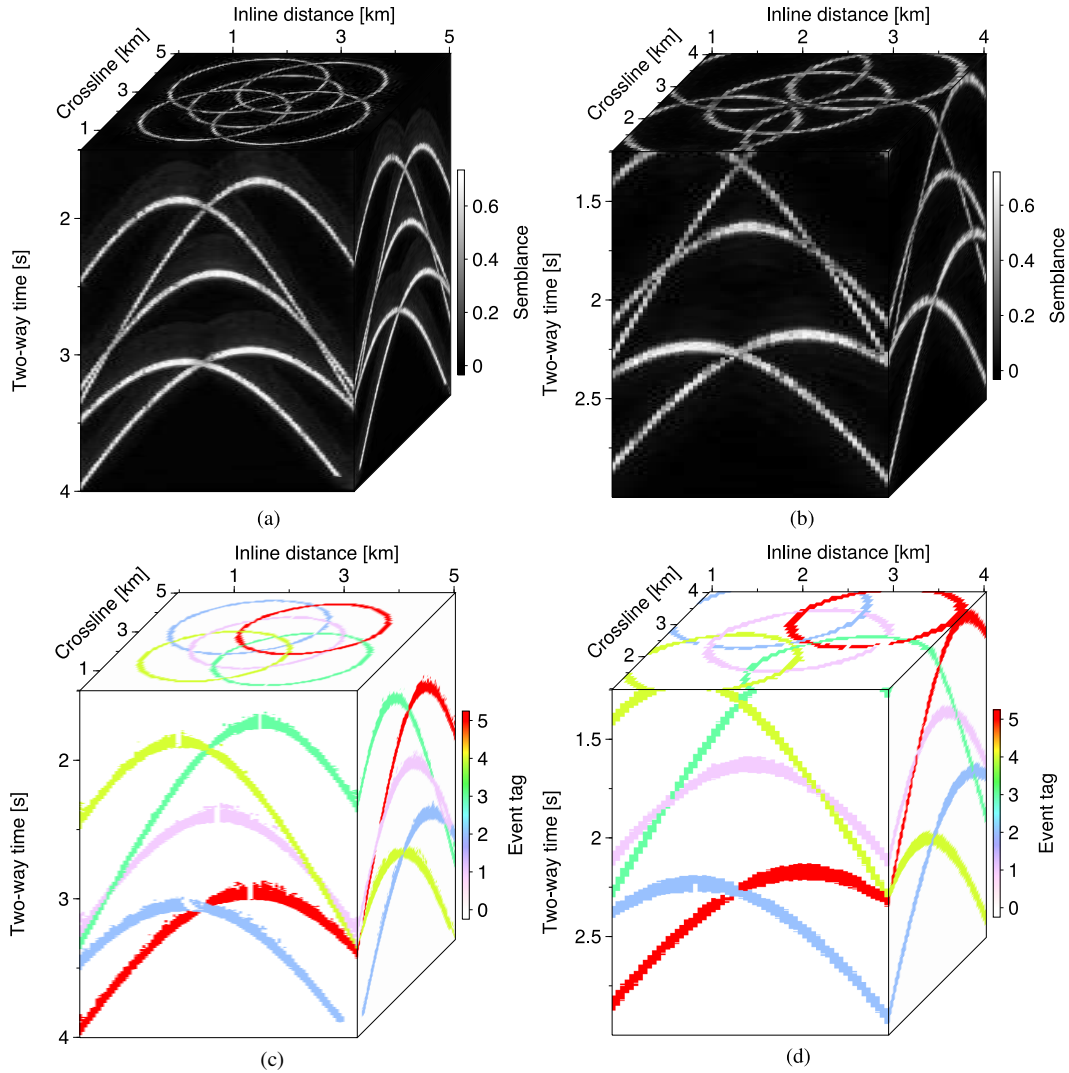


Figure 5. Results for 3D synthetic diffraction data with five events: (a) the zero-offset coherence cube, (b) an inner excerpt of the coherence cube, (c) the resulting event tag cube and (d) an excerpt of the event tag cube.

ging algorithm to synthetic 3D diffraction data. The data set contains five diffractions and is also based on a vertically inhomogeneous velocity model. While Figs 5(a) and (b) show the full zero-offset coherence volume and an inner excerpt of it, Figs 5(c) and (d) present the resulting event tags. Although some problems occurred at the apices of the diffractions, all five events could be tagged correctly. Since the number of wavefront attributes is larger in 3D, the discrimination of diffractions is even better constrained than in 2D. In contrast to the presented 2D results, for the generation of these results absolute attribute differences instead of the semblance coefficient were used. Further, the apex coordinates have not yet been incorporated into the 3D implementation.

4.3 2D field data

In Fig. 6, the results of an application of the proposed 2D event tagging algorithm to complex 2D marine field data are presented. The data set was acquired by TGS in the Eastern Mediterranean

offshore Israel. It is characterized by pronounced salt roller structures (Netzeband *et al.* 2006), which cause a lot of diffracted energy (Bauer *et al.* 2017a). The wavefront attributes for these results were obtained with a CRS implementation using global optimization and accounting for conflicting dips (Walda & Gajewski 2017). Before the application of the event tagging algorithm, a post-stack diffraction separation (Dell & Gajewski 2011) was applied to the CRS results. The full resulting zero-offset diffraction coherence section is shown in Fig. 6(a), while Fig. 6(c) presents a close-up taken from the far right part of the profile. The corresponding event tags are plotted in Fig. 6(b) as an overlay over the entire coherence and in Fig. 6(d) for the close-up. The results reveal that a large number of diffractions among the whole profile could be identified and tagged correctly. Problems only occurred in regions, where diffraction apices lie very close together resulting in very similar wavefront attributes. Please note that this result was obtained in a completely unsupervised fashion without any manual quality control involved. As an interesting by-product, the event tagging algorithm also provides a total event count.

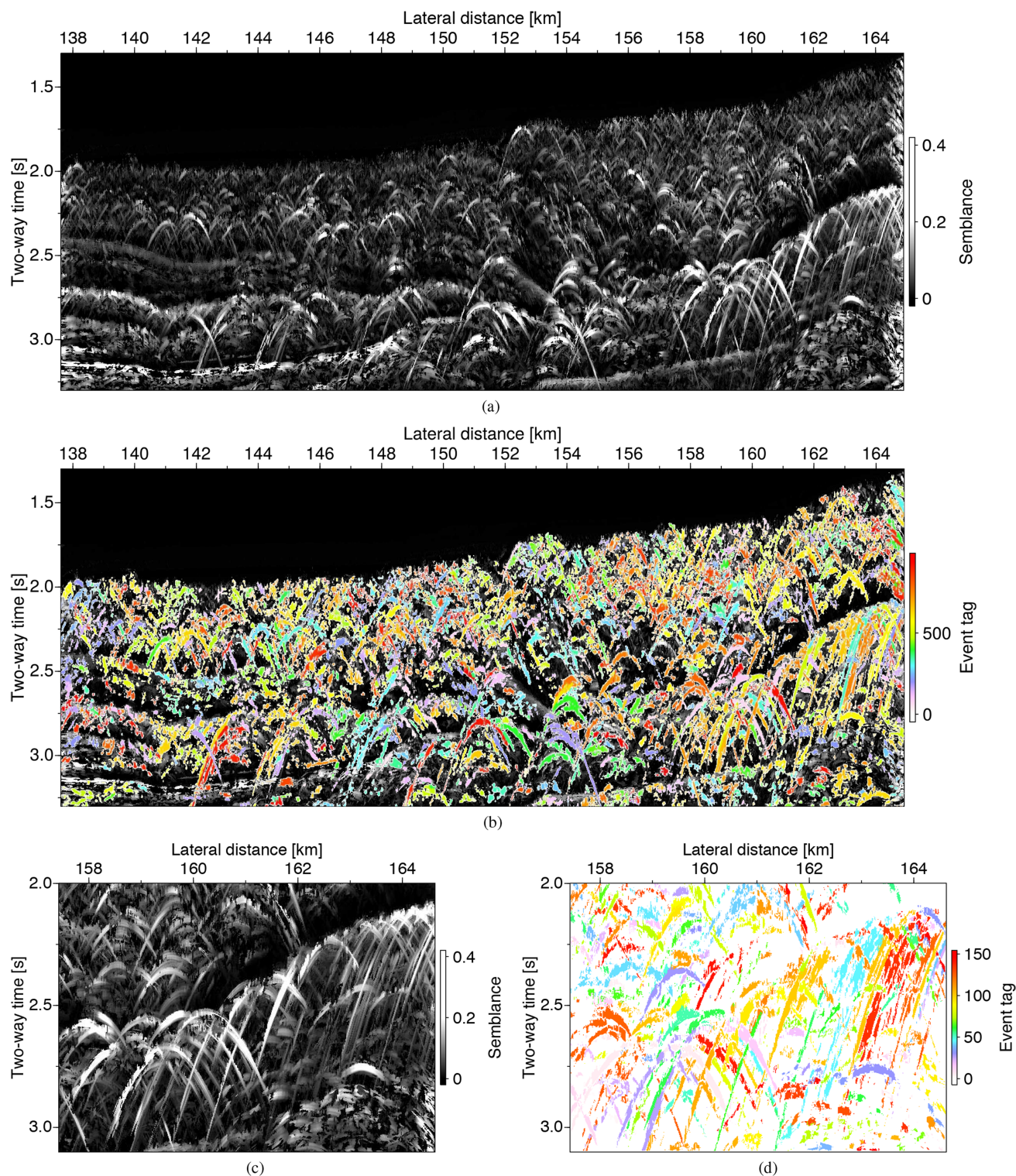


Figure 6. Results for the marine field data: (a) the zero-offset coherence after diffraction separation, (b) the coherence section overlain with resulting event tags, (c) an excerpt from the far right part of the coherence section and (d) the event tags for the same excerpt.

4.4 Potential applications

As previously outlined, various subsequent processing steps may benefit from the identification and tagging of diffractions, three of which we will outline in the following.

4.4.1 Diffraction decomposition

In the case of diffractions, that is, non-Snell scattering, one can make use of the fact that up- and downgoing waves are decoupled and therefore, the moveout of a diffraction can be described

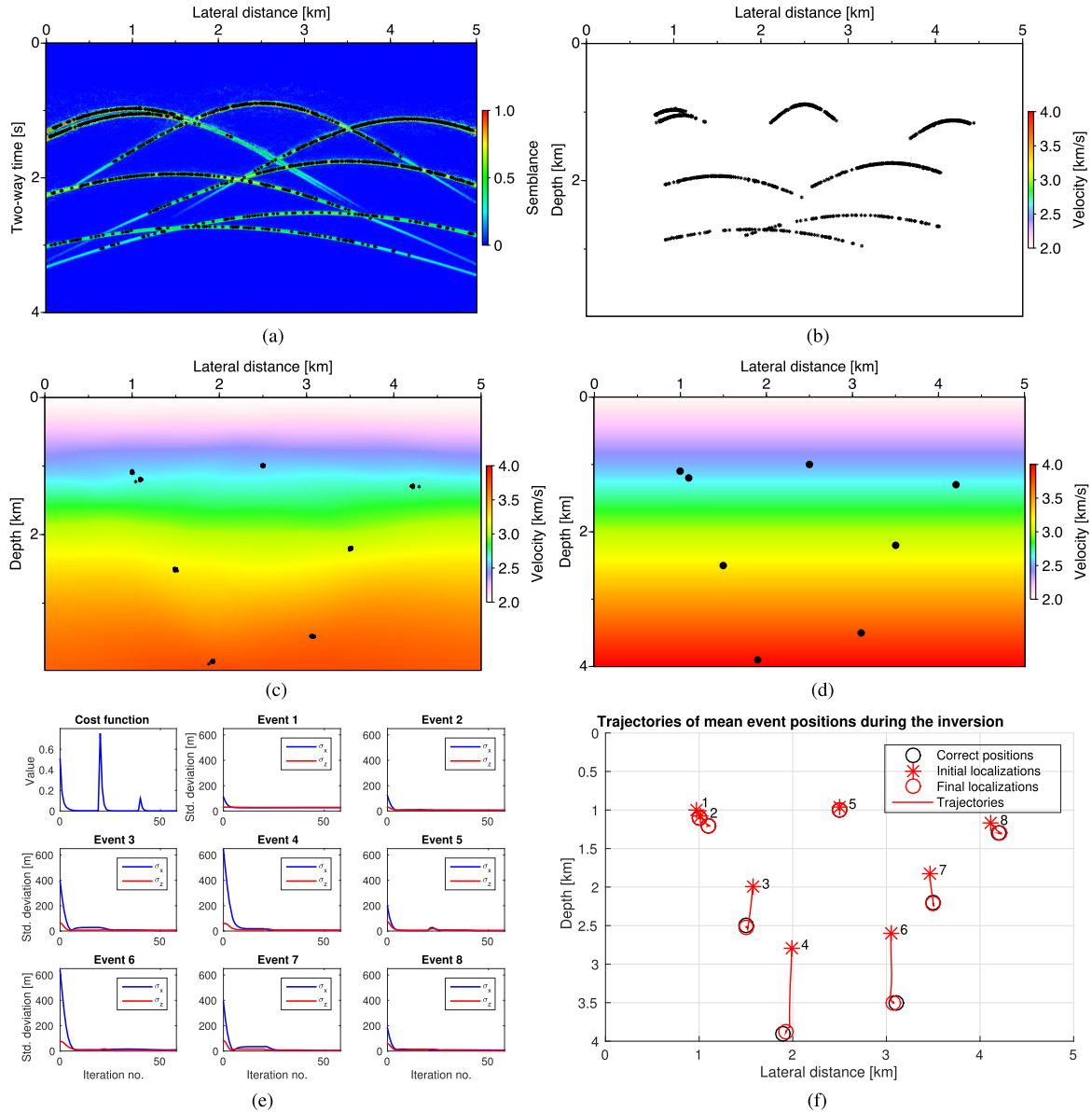


Figure 7. Application of wavefront tomography to 2D synthetic diffraction data. The picked data points are (a) the input for the inversion, (b) the constant initial model, (c) the inverted model with the final localizations of all data points and (d) the correct model with the correct diffractor positions. Panel (e) shows the cost function and the standard deviations σ_x and σ_z of all locations belonging to the same event. The peaks in the cost function correspond to refinements of the B-spline-knot grid. In panel (f), the trajectories of the mean event locations during the inversion are depicted. The red stars indicate the mean initial locations, the red circles the mean final locations and the red lines the corresponding trajectories during the inversion. The black circles are the correct locations of the diffractors.

entirely in the zero-offset setting (Bauer *et al.* 2016). This means that any finite-offset stacking operator can be composed out of two zero-offset operators extracted at the source and receiver locations corresponding to the desired offset,

$$t_{FO}(x_s^0, x_g^0, t_0^{FO}, \alpha_s, \alpha_g, R_s, R_g) = \frac{t_{ZO}(x_s^0, t_0^{ZO,s}, \alpha_0^s, R_{NIP}^s)}{2} + \frac{t_{ZO}(x_g^0, t_0^{ZO,g}, \alpha_0^g, R_{NIP}^g)}{2}, \quad (15)$$

where t_{FO} is the finite-offset operator for the half-offset $(x_g^0 - x_s^0)/2$ composed out of two independent zero-offset diffraction operators measured at x_s^0 and x_g^0 , respectively. The finite-offset wavefront attributes coincide with their zero-offset counterparts from the

corresponding source and receiver locations and the finite-offset reference traveltime t_0^{FO} is given by $(t_0^{ZO,s} + t_0^{ZO,g})/2$. Unlike the extrapolation method mentioned in Section 2.2.2, the diffraction traveltime decomposition is exact, as recently shown in theory and proven in synthetic and field data applications by Bauer *et al.* (2015, 2016). Since it depends on the unique properties of diffractions, this method is not applicable to reflection data. Event tagging is an essential ingredient for the application of diffraction decomposition, because the information, which zero-offset measurements belong to the same event, is needed in order to find the two zero-offset operators in eq. (15). If the information is available, the contributions do not have to be searched for in the data by coherence analysis, which significantly speeds up the application.

4.4.2 Wavefront tomography

Wavefront tomography (Duveneck 2004a) is an efficient and stable seismic inversion scheme, which uses zero-offset wavefront attributes for velocity model building in the depth domain. Initially, wavefront tomography was mainly applied using attributes measured for reflections (Duveneck 2004a; Dümmling *et al.* 2008). Bauer *et al.* (2017a) recently showed that diffractions can help to improve the resolution of the velocity models obtained with wavefront tomography and that their unique properties may contribute not only to further constrain the inversion, but also to estimate uncertainties (Bauer *et al.* 2017b). Further, Schwarz *et al.* (2016) have shown that wavefront tomography may likewise be used for passive seismic source localization.

Wavefront tomography is an efficient method because it does not require any interaction with the pre-stack data. The data points, which form the input for the inversion, can be picked in a completely automatic fashion in the attribute volumes estimated by the zero-offset CRS stack based on their local coherence (Bauer *et al.* 2017a). Each data point consists of the set of zero-offset attributes

$$\mathbf{d}_i = (x_0, T, p, M_{\text{NIP}})_i, \quad i = 1, \dots, n_{\text{picks}}, \quad (16)$$

where $T = t_0/2$ is the one-way zero-offset traveltime. The velocity model $v(\xi, \zeta)$ is described by B-splines, whose user-defined knot locations are given by a $n_\xi \times n_\zeta$ grid. During the inversion, kinematic ray tracing into the subsurface is performed for all data points starting from d_i to obtain initial subsurface locations (NIPs) $(\xi, \zeta, \theta)_i$, where θ is the angle at which the ray arrives at (ξ, ζ) . Subsequently, dynamic ray tracing in the upward direction starting from $(\xi, \zeta, \theta)_i$ yields modelled data points $\tilde{\mathbf{d}}_i = (\tilde{x}_0, \tilde{T}, \tilde{p}, \tilde{M}_{\text{NIP}})_i$. The least-squares misfit between measured and modelled data is used as the objective function for the inversion, which is given by

$$\Psi(\mathbf{m}) = \frac{1}{2} \|\mathbf{d} - \tilde{\mathbf{d}}\|_2^2 + \Lambda(\partial_{\xi\xi} v(\xi, \zeta), \partial_{\xi\zeta} v(\xi, \zeta)), \quad (17)$$

where \mathbf{m} is the model vector that contains the B-spline coefficients v_i and the subsurface locations $(\xi, \zeta, \theta)_i$ related to the data points. The additional regularization term Λ ensures a smooth velocity model by minimizing the second derivatives of $v(\xi, \zeta)$. In our implementation, the velocity model is updated iteratively by minimizing the misfit function $\Psi(\mathbf{m})$ using a least-squares algorithm (Paige & Saunders 1982). A working implementation of wavefront tomography in 3D is also available (Duveneck 2004b).

In the context of wavefront tomography, the event tags pave the way for an assessment of the obtained velocity models via the quantification of localization uncertainties in depth. Also, contributions which belong to the same diffraction may be forced to focus in depth by introducing a constraint into the inversion. As an example, Fig. 7 shows the results of an application of wavefront tomography to the 2D synthetic diffraction data introduced in Section 4.1. Fig. 7(a) shows the data points, which form the input for the inversion and were picked in an automatic fashion based on their coherence. The initial model (Fig. 7b) merely consists of the constant near-surface velocity used for the estimation of wavefront attributes. Black asterisks indicate the initial ray starting locations for all data points, which are obtained by kinematic ray tracing. The final model (Fig. 7c) was obtained after a total of 61 iterations. During the inversion, the initial 6×5 -grid of B-spline knots with a knot spacing of 1000 m in both x - and z -directions was refined twice by halving the knot spacing, such that the final 21×17 grid has a knot spacing of 250 m in both directions. The result shows that the final ray starting locations (black asterisks) focused at eight distinct locations, although they were treated independently in this

application, that is, no focusing constraint has been included into the inversion. A comparison to the true model with the correct positions of the eight diffractors (Fig. 7d) directly reveals that both velocity and localizations could be retrieved successfully by the inversion algorithm.

In this application, the event tags were used to calculate the mean positions and standard deviations of the depth locations connected to all data points with the same event tag during the inversion. Fig. 7(e) shows the horizontal and vertical standard deviations σ_x and σ_z for each of the eight events along with the cost function (17). The peaks in the cost function correspond to the two refinements of the B-spline grid. As expected, the standard deviations of all events decrease in a similar fashion as the cost function and converge to very small values, indicating a good localization quality. In Fig. 7(f), the trajectories of the mean event positions during the inversion are plotted. The stars indicate the mean positions in the initial model, the lines correspond to the trajectories of the mean positions during the inversion and the red circles are the mean positions in the final model. The black circles denote the correct positions of the diffractors, which are almost congruent with the final localizations for all eight events.

4.4.3 Passive-source data

Diffractions are focusing wavefields and kinematically, from a wavefront perspective, behave exactly like passive-source wavefields excited at the diffractor location. The previously described process of wavefront tomography back-projects emerging wave fronts, characterized through local coherence measurements, into the subsurface, which lets one arrive at an estimate of both, the focusing location, and the traversed velocity structure. Thus, it is likewise naturally applicable to passive seismic data (Schwarz *et al.* 2016; Diekmann *et al.* 2018). While in controlled-source acquisitions, the zero-offset response directly reveals (twice) the reference propagation time t_0 , in the passive case this quantity needs to be estimated additionally due to the fact that the excitation time t_s is generally not known. For the general 3D case we have

$$[t_{\text{data}} + t(t_0, \mathbf{m}_0) - t_0]^2 = (t_0 + \mathbf{p} \Delta \mathbf{m})^2 + t_0 \Delta \mathbf{m}^T \mathbf{N} \Delta \mathbf{m}, \quad (18)$$

where $t_{\text{data}} = t_s + t_0$ is the reference recording time and t_0 , here, represents the one-way rather than the two-way propagation time at the reference receiver location \mathbf{m}_0 . In correspondence with the general 3D paraxial two-way traveltime operator (4), $\Delta \mathbf{m}$ denotes the lateral receiver separation of every considered trace, and the quantities \mathbf{p} and \mathbf{N} represent the two-component slope vector and the 2×2 curvature matrix, respectively. As eq. (18) suggests, the propagation time t_0 and the time coordinate of the considered data point, in contrast to the controlled-source case, generally differ, thereby demanding the estimation of an additional unknown from the data. Please note, however, that the source excitation time t_s , which can directly be derived from the given recording time t_{data} and the estimated t_0 , represents a natural global event attribute that can also be used for event discrimination (Schwarz *et al.* 2016; Diekmann *et al.* 2018). In the common-source or the common-receiver gather, diffractors appear exactly like passive sources and the time of diffraction is generally not known and needs to be estimated (e.g. Schwarz & Gajewski 2017c). Similar to the example presented in the previous subsection, the application of wavefront tomography to passive seismic data benefits directly from the event tagging scheme (Diekmann *et al.* 2018).

5 DISCUSSION

A main pre-requisite for the suggested event-tagging scheme is the sufficiently dense sampling of the recorded wavefields. While user-defined constraints can help to guide the coherence analysis in cases of moderate sparsity, too large trace separations are likely to result in spatial aliasing which makes conventional coherence analysis suffer or even fail. However, this limitation is intrinsic and well-acknowledged in the general context of migration. Therefore, it is by no means exclusive to the presented method. In addition, owing to the symmetry of diffractions in different data configurations, dense trace spacing—at least in one of these domains—can be safely assumed in most realistic circumstances. If diffracted wavefields are numerous and strongly interfere with each other—an observation that can often be made, for example, in crystalline rock environments—large portions of an event might be hidden behind other, more prominent contributions, resulting in the so-called *conflicting-dip problem*, which represents a notorious challenge in multidimensional stacking (e.g. Walda & Gajewski 2017). Schwarz & Gajewski (2017b) presented a simple yet powerful solution to this problem, in that the less prominent interfering wavefields can be accessed by adaptively subtracting the amplitude-strong contributions that are normally favoured. Although only reflections were targeted, the same methodology can also be applied to adaptively separate one diffraction from another. As is the case with other methods, the estimation of local attribute similarity can be flawed if different diffractions are largely tangential, that is, of similar shape and location, in data space. While the formulation of more discriminative attribute representations and similarity measures can, to a certain extent, help to improve selectivity in these situations, natural limitations are reached when differences in onset and overall shape approach the order of the predominant signal's period. However, it may be argued that in this case, the two events from a wavefront perspective are largely equivalent and likely have originated in a similar subsurface region.

Building on the potential for full automation in coherence analysis and multidimensional stacking, the presented strategy links individual measurements of one particular diffracted event without supervision by evaluating the local similarity of a set of wavefront attribute representations. While the presented attributes turned out to already work reasonably well, they should merely be viewed as exemplary measures for discrimination. In general, the algorithm, depending on the wavefield complexity encountered in the preceding coherence analysis stage, couples to the data through these wavefront characteristics and other, more elaborate versions might be considered in the future. The unsupervised grouping or tracking of individual contributions of a data set is well-known in other fields. In image processing, a variety of sophisticated techniques exist to perform the segmentation of an image, for example, based on colour. As the colour-coded images of the presented event attributes suggest, the detection of their local similarity can be fully transformed to an image processing objective, which lets a vast ecosystem of commercial or open-source segmentation routines be readily exploitable for the discrimination of individual diffracted events. In addition, concepts from machine learning, that is, more sophisticated types of pattern recognition, should prove useful in further improving the presented results. Despite these strong and fruitful interfaces, however, it needs to be appreciated that the extracted attributes represent physically meaningful characteristics of the emerging diffracted wavefronts, which helps to naturally constrain and guide existing techniques. As illustrated with different concrete examples, we are convinced that the global identification

and tagging of individual diffracted contributions bears the potential to significantly improve existing applications, including but certainly not limited to velocity model building. We have demonstrated with a simple example that the detection of a joint origin in depth directly helps to constrain wavefront-tomographic inversion potentially leading to improved estimates of the scatterer location and the principal assessment of event-consistent uncertainties. Although not explicitly presented here, it appears natural to assume that in the same fashion, full-waveform-based as well as migration techniques are expected to equally benefit from these constraints. Note that the presented method does not intrinsically assume a type of event and thus, in principle, is applicable to any type of event. While an application to reflections is not worthwhile in the context of focusing in the subsurface, since every reflected contribution in a zero-offset section originates at a different subsurface location, in the case of edge or line diffractions it makes sense to tag their diffractive parts, which also belong to the same subsurface point. However, the reflective parts, whose directional behaviour honours Snell's law, may be neglected.

6 CONCLUSIONS

We have introduced a fully unsupervised scheme for the global identification and tagging of diffractions that stem from the same subsurface region. The proposed method works entirely in the data domain and only relies on the assumption of local similarity of wavefront attributes estimated during the CRS stack. Since wave propagation is a smoothing process, this assumption does not restrict the suggested approach to moderately heterogeneous subsurface settings. Applications to synthetic 2D and 3D diffraction data have confirmed that diffractions can be identified and tagged correctly. An application to complex marine field data further revealed the potential and stability of the method in complex settings. Future work may include the integration of sophisticated image segmentation algorithms as well as machine learning techniques into the suggested scheme. As illustrated by means of a synthetic diffraction example, the gained knowledge may be exploited to further constrain diffraction wavefront tomography by focusing common contributions in depth and to assess uncertainties in the obtained velocity models. Also, other processing steps such as time migration and pre-stack diffraction enhancement may benefit from the proposed event tagging scheme. In addition, the suggested scheme is likewise applicable to passive seismic data.

ACKNOWLEDGEMENTS

We thank Leon Diekmann for fruitful discussions and Jan Walda for the generation of wavefront attributes for the marine field data. This work was kindly supported by the Federal Ministry for Economic Affairs and Energy of Germany (BMW, 03SX427B) and by the sponsors of the Wave Inversion Technology (WIT) consortium, Hamburg, Germany. B. Schwarz is supported by a research fellowship of the German Research Foundation (DFG, SCHW 1870/1-1). We thank the Applied Seismics Group at the University of Hamburg for continuous discussion and TGS for providing the marine field data. We thank Andrej Bóna, one anonymous reviewer and the Associate Editor Jean Virieux for their helpful comments during the revision process.

REFERENCES

- Bakhtiari Rad, P., Schwarz, B., Gajewski, D. & Vanelle, C., 2018. Common-reflection-surface-based prestack diffraction separation and imaging, *Geophysics*, **83**(1), S47–S55.
- Bauer, A., Schwarz, B. & Gajewski, D., 2015. Prestack diffraction enhancement using a traveltimes decomposition approach, in *SEG Technical Program Expanded Abstracts 2015*, pp. 3820–3824, Society of Exploration Geophysicists.
- Bauer, A., Schwarz, B. & Gajewski, D., 2016. Enhancement of prestack diffraction data and attributes using a traveltimes decomposition approach, *Stud. Geophys. Geod.*, **60**(3), 471–486.
- Bauer, A., Schwarz, B. & Gajewski, D., 2017a. Utilizing diffractions in wavefront tomography, *Geophysics*, **82**(2), R65–R73.
- Bauer, A., Schwarz, B. & Gajewski, D., 2017b. Quantifying diffracted and passive event location uncertainties with local wavefront measurements, in *79th EAGE Conference and Exhibition 2017*, EAGE.
- Baykulov, M. & Gajewski, D., 2009. Prestack seismic data enhancement with partial common-reflection-surface (CRS) stack, *Geophysics*, **74**(3), V49–V58.
- Bóna, A., 2011. Shot-gather time migration of planar reflectors without velocity model, *Geophysics*, **76**(2), S93–S101.
- Dafni, R. & Symes, W.W., 2017. Diffraction imaging by prestack reverse-time migration in the dip-angle domain, *Geophys. Prospect.*, **65**(S1), 295–316.
- Dell, S. & Gajewski, D., 2011. Common-reflection-surface-based workflow for diffraction imaging, *Geophysics*, **76**(5), S187–S195.
- Diekmann, L., Schwarz, B., Bauer, A. & Gajewski, D., 2018. Source localisation and joint velocity model building, in *80th EAGE Conference and Exhibition 2018*, EAGE.
- Dümmong, S., Meier, K., Gajewski, D. & Hübscher, C., 2008. Comparison of prestack stereotomography and NIP wave tomography for velocity model building: instances from the Messinian evaporites, *Geophysics*, **73**(5), VE291–VE302.
- Duveneck, E., 2004a. Velocity model estimation with data-derived wavefront attributes, *Geophysics*, **69**(1), 265–274.
- Duveneck, E., 2004b. 3D tomographic velocity model estimation with kinematic wavefield attributes, *Geophys. Prospect.*, **52**(6), 535–545.
- Fomel, S., 2002. Applications of plane-wave destruction filters, *Geophysics*, **67**(6), 1946–1960.
- Fomel, S. & Kazinnik, R., 2013. Non-hyperbolic common reflection surface, *Geophys. Prospect.*, **61**(1), 21–27.
- Fomel, S., Landa, E. & Taner, M.T., 2007. Poststack velocity analysis by separation and imaging of seismic diffractions, *Geophysics*, **72**(6), U89–U94.
- Gelchinsky, B., Berkovitch, A. & Keydar, S., 1999. Multifocusing homeomorphic imaging: Part 1. basic concepts and formulas, *J. Appl. Geophys.*, **42**(3), 229–242.
- Hubral, P., 1983. Computing true amplitude reflections in a laterally inhomogeneous earth, *Geophysics*, **48**, 1051–1062.
- Jäger, R., Mann, J., Höcht, G. & Hubral, P., 2001. Common-reflection-surface stack: Image and attributes, *Geophysics*, **66**, 97–109.
- Khaidukov, V., Landa, E. & Moser, T.J., 2004. Diffraction imaging by focusing-defocusing: an outlook on seismic superresolution, *Geophysics*, **69**(6), 1478–1490.
- Klokov, A. & Fomel, S., 2012. Separation and imaging of seismic diffractions using migrated dip-angle gathers, *Geophysics*, **77**(6), S131–S143.
- Kozlov, E., Barasky, N., Korolev, E., Antonenko, A. & Koshchuk, E., 2004. Imaging scattering objects masked by specular reflections, in *SEG Technical Program Expanded Abstracts 2004*, pp. 1131–1134, Society of Exploration Geophysicists.
- Krey, T., 1952. The significance of diffraction in the investigation of faults, *Geophysics*, **17**(4), 843–858.
- Landa, E. & Keydar, S., 1998. Seismic monitoring of diffraction images for detection of local heterogeneities, *Geophysics*, **63**(3), 1093–1100.
- Mann, J., 2002. Extensions and applications of the common-reflection-surface stack method, *Ph.D. thesis*, University of Karlsruhe.
- Moser, T.J. & Howard, C.B., 2008. Diffraction imaging in depth, *Geophys. Prospect.*, **56**(5), 627–641.
- Müller, N.-A., 2009. Treatment of conflicting dips in the 3D common-reflection-surface stack, *Geophys. Prospect.*, **57**(6), 981–995.
- Neidell, N.S. & Taner, M.T., 1971. Semblance and other coherency measures for multichannel data, *Geophysics*, **36**(3), 482–497.
- Netzeband, G., Hübscher, C. & Gajewski, D., 2006. The structural evolution of the Messinian evaporites in the Levantine Basin, *Mar. Geol.*, **230**(3), 249–273.
- Paige, C.C. & Saunders, M.A., 1982. LSQR: an algorithm for sparse linear equations and sparse least squares, *ACM Trans. Math. Softw.*, **8**(1), 43–71.
- Santos, L.A., Mansur, W.J. & McMechan, G.A., 2012. Tomography of diffraction-based focusing operators, *Geophysics*, **77**(5), R217–R225.
- Schwarz, B. & Gajewski, D., 2017a. The two faces of NMO, *Leading Edge*, **36**(6), 512–517.
- Schwarz, B. & Gajewski, D., 2017b. Accessing the diffracted wavefield by coherent subtraction, *Geophys. J. Int.*, **211**(1), 45–49.
- Schwarz, B. & Gajewski, D., 2017c. A generalized view on normal moveout, *Geophysics*, **82**(5), V335–V349.
- Schwarz, B., Vanelle, C., Gajewski, D. & Kashtan, B., 2014. Curvatures and inhomogeneities: an improved common-reflection-surface approach, *Geophysics*, **79**(5), S231–S240.
- Schwarz, B., Vanelle, C., Wißmath, S., Bauer, A. & Gajewski, D., 2015. Efficient common-reflection-surface-based prestack slope determination for stereotomography, in *SEG Technical Program Expanded Abstracts 2015*, pp. 5248–5253, Society of Exploration Geophysicists.
- Schwarz, B., Bauer, A. & Gajewski, D., 2016. Passive seismic source localization via common-reflection-surface attributes, *Stud. Geophys. Geod.*, **60**(3), 531–546.
- Schwarz, B., Bauer, A. & Gajewski, D., 2017. Automated single-channel data inversion using diffractions, in *79th EAGE Conference and Exhibition 2017*, EAGE.
- Walda, J. & Gajewski, D., 2017. Determination of wavefront attributes by differential evolution in the presence of conflicting dips, *Geophysics*, **82**(4), V229–V239.
- Walda, J., Schwarz, B. & Gajewski, D., 2017. A competitive comparison of multiparameter stacking operators, *Geophysics*, **82**(4), V275–V283.
- Zhang, Y., Bergler, S. & Hubral, P., 2001. Common-reflection-surface (CRS) stack for common offset, *Geophys. Prospect.*, **49**, 709–718.